Inorganic Chemistry

Article

pubs.acs.org/IC

Optical Activity and Dehydration-Driven Switching of Magnetic Properties in Enantiopure Cyanido-Bridged $Co^{II}_3W^{V}_2$ Trigonal Bipyramids

Szymon Chorazy,[†] Robert Podgajny,*[,†] Wojciech Nogaś,[†] Szymon Buda,[†] Wojciech Nitek,[†] Jacek Mlynarski,[†] Michał Rams,[‡] Marcin Kozieł,[†] Ewa Juszyńska Gałązka,[§] Veacheslav Vieru,[⊥] Liviu F. Chibotaru,[⊥] and Barbara Sieklucka[†]

[†]Faculty of Chemistry, Jagiellonian University, Ingardena 3, 30-060 Kraków, Poland

[‡]Institute of Physics, Jagiellonian University, Łojasiewicza 11, 30-348 Kraków, Poland

[§]H. Niewodniczański Institute of Nuclear Physics, Polish Acedemy of Sciences, Radzikowskiego 152, 31-342 Kraków, Poland

[⊥]Theory of Nanomaterials Group and Institute of Nanoscale Physics and Chemistry, Katholieke Universiteit Leuven, Celestijnenlaan 200F, 3001 Heverlee, Belgium

Supporting Information

ABSTRACT: The unique enantiopure $\{[\Lambda\text{-}Co^{II}((R)\text{-mpm})_2]_3[W^{V}(CN)_8]_2\}\cdot 9H_2O$ [(*R*)-**1**] and $\{[\Delta\text{-}Co^{II}((S)\text{-mpm})_2]_3[W^{V}(CN)_8]_2\}\cdot 9H_2O$ [(*S*)-**1**], where mpm = α-methylpyridinemethanol, magnetic spongelike materials, crystallizing in the chiral $P2_1$ space group, are constructed of cyanido-bridged $\{Co_3W_2\}$ trigonal bipyramids with three *cis*-$[Co^{II}(mpm)_2(\mu\text{-}NC)_2]$ moieties in equatorial sites and two $[W^{V}(CN)_8]^{3-}$ units in apical positions. The arrangement of $\{Co_3W_2\}$ clusters in the crystal lattice is controlled by interactions with crystallization H_2O molecules, resulting in two independent hydrogen-bonding systems: the first weaving along open channels in the *a* direction (weakly bonded H_2O) and the second closed in the cages formed by the surrounding $[W(CN)_8]^{3-}$ and mpm fragments (strongly bonded H_2O). The strong optical activity of (*R*)- and (*S*)-**1** together with continuous chirality measure (CCM) analysis confirms the chirality transfer from enantiopure (*R*)- and (*S*)-mpm to $[Co(mpm)_2(\mu\text{-}NC)_2]$ units, a cyanido-bridged skeleton, and to the whole crystal lattice. Magnetic properties confronted with ab initio calculations prove the ferromagnetic couplings within Co^{II}–NC–W^{V} linkages inside $\{Co_3W_2\}$ molecules, accompanied by weak antiferromagnetic intermolecular interactions. The reversible removal of weakly bonded H_2O above 50 °C induces the structural phase transition **1** ⇄ **1deh** and strongly affects the magnetic characteristics. The observed changes can be interpreted in terms of the combined effects of the decreasing strength of ferromagnetic Co^{II}–W^{V} coupling and the increasing role of antiferromagnetic intermolecular correlation, both connected with dehydration-induced structural modifications in the clusters' core and supramolecular network of **1**.

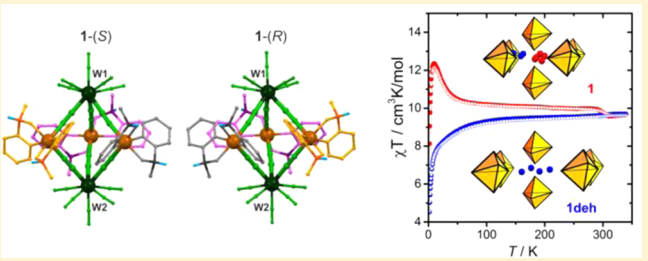

INTRODUCTION

The solid-state responsive molecular magnetic materials combining magnetism with other chemical and physical properties, such as chirality, light absorption, electron transfer, or charge transfer assisted by guest inclusion and structural transformation, create a platform for tuning, switching, and overall control of the magnetic and magnetooptical states.[1−4] This area has been recently explored, with noteworthy attention paid to the *extended* polycyanidometallate-based networks.[3,4] The implementation of chirality into cyanido-based magnets results in the observation of natural optical activity,[5−10] combined with the magnetic optical activity enhanced in the magnetically ordered phase, as reported for enantiopure $Mn^{II}[Cr^{III}(CN)_6]^{3-}$ and $Mn^{II}[Nb^{IV}(CN)_8]^{4-}$ ferrimagnets.[11,12] The combination of magnetic ordering and noncentrosymmetricity gave the extraordinary cooperative effects of magnetic second harmonic generation[8,11] and multiferroicity.[12] Other functionalities, such as luminescence and proton conductivity, were also found in cyanido-bridged assemblies.[6,7,13] The magnetic properties of polycyanidometallate systems can be efficiently controlled by external stimuli, such as pressure,[14] guest molecules,[15,16] or light.[8,17−19] The guest responsive systems represent a remarkable class of functional magnetic materials because the reversible introduction of small molecules into the microporous network can modify the strength of magnetic interactions, leading to a dramatic shift in T_c of magnetic ordering.[16,20−22]

As a part of our research program, we consider the exploration of low-dimensional systems based on a M–CN–

Received: February 27, 2015
Published: May 28, 2015

DOI: 10.1021/acs.inorgchem.5b00470
Inorg. Chem. 2015, 54, 5784−5794

M′ linkage with nontrivial properties as a potential platform for functionality.[23] The CN^--bridged molecules adopt various discrete topologies controlled by a range of blocking ligands.[24] This includes trinuclear M_2M',[25,26] tetranuclear $M_2M'_2$,[27,28] octanuclear $M_4M'_4$,[29,30] pentanuclear $M_3M'_2$,[31] and pentadecanuclear $M_9M'_6$ clusters.[32−35] Among them, special attention is paid to trigonal-bipyramidal (TBP) $M_3M'_2$ clusters, realized by two axial polycyanidometallates forming bridges to three equatorial metal centers of octahedral geometry with four coordination sites blocked by chelating ligands.[31] The TBP clusters are usually obtained by the combination of $[M^{III}(CN)_6]^{3-}$ (M = Cr, Fe, Co, Mo, Os) ions and complexes of divalent 3d metal ions with diimine blocking ligands (e.g., tmphen = 3,4,7,8-tetramethyl-1,10-phenanthroline).[31,36] The few TBP molecules are built of tricyanidometallates,[37,38] and those of the octacyanidometallate family are represented only by $\{[Ni^{II}(tmphen)_2]_3[M^{V}(CN)_8]_2\}$ (M = Mo, W).[39] The cyanido-bridged TBP-based crystalline solids exhibit a number of magnetic and optical functionalities, including both high-spin molecules,[40,41] single-molecule magnet (SMM) behavior,[37,42] thermal-induced and photoinduced SCO and CTIST phenomena,[43−45] and linkage isomerism.[31,36] Because of the relatively stable molecular geometry and well-defined positions of the metal centers, a TBP core was found to be an attractive platform for the theoretical investigation of spin transitions and cyanido-mediated magnetic coupling.[31,46,47]

In this context, of particular interest is the incorporation of chirality into magnetic TBP clusters. The enantiopure character originating from the Δ or Λ chiral configuration of equatorial $[M^{II}(L)_2(NC)_2]$ units in $M_3M'_2$ clusters is preferred because of the specific geometry of a cluster core and the steric effect on organic ligands L, which creates a good starting point toward the chiral structures and lattices. In fact, some of the reported crystal structures contain chiral ΔΔΔ or ΛΛΛ clusters, but the unit cell includes an equal number of each enantiomer, resulting in a centrosymmetric space group.[31] Only very rare examples of the enantiomorphic space group due to the spontaneous resolution connected with the steric hindrance on blocking organic ligands were shown in the cyanido-bridged TBP family,[36,48,49] whereas no report on the optical activity was presented. Moreover, TBP clusters create the dynamic supramolecular networks of tunable properties upon the reversible addition/removal of solvent. Dunbar et al. showed a great sensitivity of the electronic spin state of $\{[Co^{II/III}(tmphen)_2]_3[Fe^{II/III}(CN)_6]\}$ clusters to the degree of solvation.[43] Depending on the presence of water or acetonitrile in the intercluster space, Co_3Fe_2 molecules existed as different electronic isomers, and only some of them reveal thermally induced spin transition. Thus, the implementation of chirality into the dynamic $M_3M'_2$ assemblies designates them to be potentially used as rudimentary platforms for the overall control of the magnetooptical states of magnetic sponges.

Accordingly, we have focused on the design and synthesis of a dynamic chiral magnetic supramolecular network based on TBP clusters. Exploiting our experience in the area of octacyanidometallates,[4] we used cobalt(II) complexes with $[W^{V}(CN)_8]^{3-}$ ions as the building blocks, ensuring the 3:2 ratio between metal centers and TBP topology, along with an appropriate blocking ligand,[1] to induce chirality. We applied the enantiopure bidentate (*R*)- or (*S*)-α-methyl-2-pyridinemethanol (mpm), which was shown to be an efficient ligand to build a chiral $Mn^{II}[Nb^{IV}(CN)_8]^{4-}$ coordination network.[10] Here, we present the synthesis, crystal structure, and optical and magnetic property studies of a pair of enantiomorphic $\{[\Lambda\text{-}Co^{II}((R)\text{-mpm})_2]_3[W^{V}(CN)_8]_2\}\cdot 9H_2O$ [(*R*)-**1**] and $\{[\Delta\text{-}Co^{II}((S)\text{-mpm})_2]_3[W^{V}(CN)_8]_2\}\cdot 9H_2O$ [(*R*)-**1**] materials built of cyanido-bridged trigonal bipyramids, exhibiting natural optical activity because of their chiral structure and dehydration-driven tuning of the magnetic properties, investigated with support of ab initio calculations.

EXPERIMENTAL SECTION

Starting Materials. $Co^{II}Cl_2\cdot 6H_2O$ and methanol used during the synthesis were purchased from commercial sources (Sigma-Aldrich, Idalia, CO) and used without further purification. $Na_3[W^{V}(CN)_8]\cdot 4H_2O$ was prepared following a literature procedure.[50] (*R*)-α-Methyl-2-pyridinemethanol [(*R*)-mpm] and (*S*)-α-methyl-2-pyridinemethanol [(*S*)-mpm] were synthesized by modification of the published procedure (see below).[51] The organic reagents 2-acetylopyridine, formic acid, and triethylamine and the catalysts [RuCl(*p*-cymene)][(*R*,*R*)-Ts-DPEN] [(*R*,*R*)-Ru-**L**] and [RuCl(*p*-cymene)][(*S*,*S*)-Ts-DPEN] [(*S*,*S*)-Ru-**L**] (Scheme 1) were purchased from Sigma-Aldrich and used without purification.

Scheme 1. Applied Synthetic Procedure toward Chiral Organic Ligands, (*R*)- and (*S*)-mpm, Used in the Construction of (*R*)- and (*S*)-1

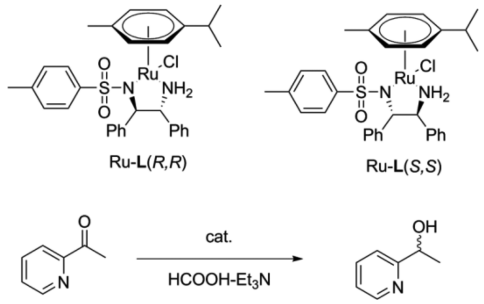

Synthesis. *1. Synthesis of (R)-α-Methyl-2-pyridinemethanol [(R)-mpm] and (S)-α-Methyl-2-pyridinemethanol [(S)-mpm].* All reactions were carried out under an argon atmosphere using standard Schlenk techniques. All glassware was oven-dried for at least 1 h before use. Commercially available catalyst (*R*,*R*)-Ru-**L** (0.062 mmol, 39.4 mg) was dissolved in 40 mL of a degassed formic acid/triethylamine mixture (molar ratio F/T = 0.2) and vigorously stirred for 5 min at 40 °C under argon. A total of 3 g of 2-acetylpyridine (24.7 mmol, 2.72 mL) was added in one portion. The reaction was monitored by thin-layer chromatography. After substrate consumption, the reaction mixture was cooled to room temperature and diluted with water (10 mL). The water phase was extracted with CH_2Cl_2 (3 × 40 mL), dried over Na_2SO_4, filtered, and concentrated. Dark-brown oil was purified by bulb-to-bulb distillation to give pure *R*-mpm (1.68 g, 55%). Enantiomeric excess (ee) of *R*-mpm was determined by high-performance liquid chromatography (Daicel Chiralcel OD column, 4.6 mm i.d. × 250 mm; eluent = 6:94 isopropyl alcohol/hexane; *T* = 21 °C; flow rate = 1.0 mL; λ = 254 nm; t_r = 12.74 (*R* isomer) and 13.35 (*S* isomer); 98% ee *R*. $[\alpha]^{26}_D$ = +26.1 (0.950, $CHCl_3$). ^{1}H NMR (300 MHz, $CDCl_3$): δ 8.47 (ddd, *J* = 4.9, 1.8, and 1.0 Hz, 1H), 7.66 (td, *J* = 7.7 and 1.8 Hz, 1H), 7.34 (dd, *J* = 7.7 and 1.0 Hz, 1H), 7.15 (ddd, *J* = 7.7, 4.9, and 1.0 Hz, 1H), 4.91 (s, 1H, OH), 4.89 (q, *J* = 6.5 Hz, 1H), 1.49 (d, *J* = 6.5 Hz, 3H). ^{13}C NMR (75 MHz, $CDCl_3$): δ 163.6, 148.0, 136.8, 122.1, 119.7, 69.2, 24.1. EI MS: 122.25 (18%), 108.24 (100%), 106.25 (43%), 79.12 (40%). For the enantiomeric catalyst (*S*,*S*)-Ru-**L**, an analogous procedure was used. (*S*)-mpm was isolated with 61% yield and 99% ee. $[\alpha]^{27}_D$ = −26.6° (*c* = 0.975, $CHCl_3$). Scheme 1 presents the applied procedure for the syntheses of (*R*)- and (*S*)-mpm.

2. Synthesis of (R)- and (S)-1. Aqueous solutions of 38.4 mg of $Na_3[W(CN)_8]\cdot 4H_2O$ (6 mL), 25.6 mg of $CoCl_2\cdot 6H_2O$ (3 mL), and 75

DOI: 10.1021/acs.inorgchem.5b00470
Inorg. Chem. 2015, 54, 5784−5794

Table 1. Crystal Data and Structure Refinement for (*S*)- and (*R*)-1

	(*R*)-**1**	(*S*)-**1**
method	single-crystal XRD	single-crystal XRD
formula	$Co_3W_2C_{58}H_{54}N_{22}O_{15}$	$Co_3W_2C_{58}H_{54}N_{22}O_{15}$
formula weight [g·mol^{-1}]	1843.72	1843.72
T [K]	293(2)	293(2)
λ [Å]	0.71073 (Mo Kα)	0.71073 (Mo Kα)
cryst syst	monoclinic	monoclinic
space group	$P2_1$	$P2_1$
a [Å]	13.650(5)	13.645(3)
b [Å]	19.840(5)	19.826(4)
c [Å]	14.794(5)	14.811(3)
β [deg]	104.169(5)	104.18(3)
V [Å^3]	3885(2)	3884.4(14)
Z	2	2
calcd density [g·cm^{-3}]	1.576	1.576
abs coeff [cm^{-1}]	3.648	3.648
F(000)	1810	1810
crysta size [mm^3]	0.35 × 0.30 × 0.15	0.30 × 0.25 × 0.20
θ range [deg]	3.02−25.00	3.39−30.00
limiting indices	$-14 < h < 16$	$-19 < h < 19$
	$-23 < k < 23$	$-27 < k < 26$
	$-14 < l < 17$	$-18 < l < 20$
collected reflns	23172	54684
unique reflns	13483	20858
R_{int}	0.0283	0.0392
completeness [%]	99.8	99.8
refinement method	full-matrix least squares on F^2	full-matrix least squares on F^2
data/restraints/param	13483/37/931	20858/37/931
Flack parameter	−0.004(5)	−0.023(4)
GOF on F^2	0.952	1.043
final R indices	R1 = 0.0312 [$I > 2\sigma(I)$], wR2 = 0.0693 (all data)	R1 = 0.0343 [$I > 2\sigma(I)$], wR2 = 0.0789 (all data)
largest diff peak and hole [e·A^{-3}]	+1.733 and −0.656	+0.965 and −0.582

mg of (*S*)- or (*R*)-mpm enantiomer (9 mL) were mixed together. A total of 0.7 g of glycerin was added and dissolved. The reaction mixture was left in a water bath at 28 °C for crystallization. Several dark-crimson crystals grew within 2 weeks. The yield was enhanced up to 60% (26 mg of product) in the presence of a small amount of crystals of the previously synthesized product in the reaction mixture because of commencement of the crystallization process. Elemental analyses gave identical results, and the representative data are presented below. Calcd for $C_{58}H_{72}Co_3N_{22}O_5W_2$ (M_{mol} = 1826 g·mol^{-1}): C, 37.4; H, 3.9; N, 16.6. Found: C, 37.2; H, 3.9; N, 16.4. IR (dry crystals in air, RT, KBr): 2192m, 2181m, 2166w, 2153 (sh), 2147m ν(C≡N); 1571m, 1488m, 1439s, 1380m, 1337m ν(C═N); 1099s, 1055s, 1015s ν(C−O); 1271m, 1160m δ(C−H); 900w, 770m γ(C−H) and aromatic ring deformation. A water δ(O−H) signal appeared at 1609 cm^{-1}.

Crystal Structure Solution and Refinement. Single-crystal diffraction data of (*S*)-**1** were collected on an Oxford Diffraction Gemini A Ultra diffractometer with graphite-monochromated Mo Kα radiation and a CCD Atlas detector, while X-ray measurements for (*R*)-**1** was performed on an Oxford Diffraction SuperNova diffractometer with graphite-monochromated Mo Kα radiation and a CCD Atlas detector. The crystal structures for both (*S*)- and (*R*)-**1** were solved by a direct method using *SHELXS-97* and refined by a full-matrix least-squares technique using *SHELXL-97*.[52a,b] Calculations were performed using a *WinGX* (version 1.80.05) integrated system.[52c] The non-H atoms were refined anisotropically and the H atoms isotropically. The positions of the H atoms for OH groups of (*R*)- and (*S*)-mpm were found using the Fourier difference density map, while all other H atoms were calculated and refined using the riding model. Restraints on the O−H distances for the hydroxyl groups of mpm ligands were applied in order to maintain the proper geometry. ISOR restraints on the thermal ellipsoids of O atoms of some H_2O solvent molecules and some C atoms of mpm ligands were also used to ensure convergence of the refinement process. The refinement process was completely analogous for (*S*)- and (*R*)-**1**, and the same restraints were applied (Table 1). Structural diagrams were prepared using *Mercury 2.3* software.[52d]

Physical Techniques. Elemental analyses of C, H, and N were performed using an EuroEA EuroVector elemental analyzer. Thermogravimetric data in the temperature range of 25−400 °C were collected on a Mettler Toledo TGA/SDTA 851^e micro-thermogravimeter at a heating rate of 1 °C·min^{-1} in an argon atmosphere. IR spectra were recorded on dried crystals in the range of 4000−550 cm^{-1} using a Thermo Scientific Nicolet iS5 spectrometer equipped with iD5 ATR-Diamond. Variable-temperature IR spectra were recorded using an Excalibur FTS-3000 spectrometer. During the experiments, the spectrometer was purged with dry nitrogen. The samples were sandwiched between two KRS-5 window disks. Powder X-ray diffraction (XRD) patterns over the 2θ range of 5−60° were collected using a PANalytical X'pert PRO MPD diffractometer equipped with a copper X-ray source ($\lambda_{K\alpha}$ = 1.5418 Å). Temperature-dependent measurements were performed using an Anton Paar TTK-450 chamber in heating mode (Bragg−Brentano geometry). The diffractograms measured at 360 K were indexed using *Expo2014* software.[53] The UV/vis absorption spectra were measured on a PerkinElmer Lambda 35 spectrophotometer, using $BaSO_4$ pellets as the reference background for the solid-state materials. Variable-temperature reflectance spectra were measured on a Avantes AvaSpec-2048 spectrometer. Natural circular dichroism (NCD) spectra for the solid state (dispersed in Nujol, 5−10 mg per several drops, and introduced between two CaF_2 plates) and mother solutions were collected using a Jasco J-810 spectropolarimeter. The recorded signals

DOI: 10.1021/acs.inorgchem.5b00470
Inorg. Chem. 2015, 54, 5784−5794

were corrected using the blank Nujol signal. Magnetic measurements were performed using Quantum Design MPMS-XL. Because of easy dehydration of the examined compounds around room temperature, the sample was inserted into the magnetometer at 250 K and the sample cavity was evacuated after sample freezing. All presented temperature dependencies were registered during sample warming. The powder sample had the form of a pressed pellet wrapped in poly(tetrafluoroethylene) tape to avoid grain rotation at an elevated magnetic field. All of these precautions were necessary to obtain a consistent set of data. The magnetic data were corrected for the diamagnetic contribution using Pascal constants.[54]

Ab Initio Calculations. All fragment ab initio calculations have been carried out with the *MOLCAS 7.8* program and are of the CASSCF/SO-RASSI/SINGLE_ANISO type.[55] Two different basis sets have been used to check the stability of the obtained results (see Table S6 in the Supporting Information, SI). The Cholesky decomposition threshold was set to 0.5×10^{-7}. Because of the computer power limitations, the calculated fragments were reduced for each Co ion, as shown in Figure S5 in the SI. The neighboring W^V atoms were replaced with Ta^V, which are diamagnetic. To test the importance of dynamical correlation effects, CASPT2 calculations[56] were done for one Co fragment using the structure shown in Figure S6 in the SI. In this case, the W atoms were substituted for La^{3+} AIMP. W ions were not calculated and were considered isotropic. The exchange coupling interactions were considered within the Lines model[57] using POLY_ANISO[58] based on the previously obtained ab initio results from SINGLE_ANISO.

RESULTS AND DISCUSSION

Crystal Structures. Both enantiomorphic materials (*R*)- and (*S*)-**1** crystallize as dark-red air-stable crystals in the space group $P\,2_1$. The unit cell consists of two cyanido-bridged $\{Co_3W_2\}$ cage molecules and 18 crystallization H_2O molecules (Figures 1 and S1 and S2 in the SI). The most important bond lengths and angles are presented in Table S2 in the SI. All atoms in the $\{Co_3W_2\}$ clusters are symmetrically non-equivalent. A single cluster has the shape of a trigonal bipyramid, with all Co ions in the equatorial plane and bridging $W(CN)_8$ ions in the axial positions. A slight distortion from the ideal TBP geometry is represented by the isosceles character of the equatorial triangle Co1Co2Co3, where the Co3 site is the distinguished one. This is illustrated by the Co1···Co3 and Co2···Co3 distances (6.66 and 6.69 Å) being significantly longer than the Co1···Co2 (6.34 Å) distance and by the differences between the relevant W···Co distances and Co···Co···Co, Co···W···Co, and W···Co···W angles (Table S1 in the SI) as well as by the differences in some of the Co−N−C_{CN}, N_{CN}−Co−N_{CN}, and N_{mpm}−Co−N_{mpm} angles (Table S2 in the SI). Both $[W(CN)_8]$ units have a geometry close to that of SAPR-8 but with different degrees of distortion from the ideal polyhedron, a minimum for W2, as illustrated by the shape measure $S_{SAPR\text{-}8} = 0.2$, and higher for W1, as illustrated by $S_{SAPR\text{-}8} = 0.45$ (Table S3 in the SI).[59] Each Co^{II} center has distorted octahedral surroundings with two chelating mpm ligands and two CN^- bridges of $[W(CN)_8]^{3-}$ arranged in cis fashion. Co centers have Co−N_{CN} bond lengths in the range of 2.064−2.113 Å and the respective C−N−Co angles in the range of 168.6−178.4° (Table S2 in the SI).

The intrinsic chirality of (*S*)- and (*R*)-mpm based on asymmetric carbon with four different groups attached (phenyl, hydroxyl, methyl, and hydrogen) is efficiently transferred[60] to the whole crystal structure (Figure 2). (*S*)-mpm embedded in (*S*)-**1** induces exclusively the right-handed helicity and the Δ absolute configuration for Co^{II} units, while (*R*)-mpm in (*R*)-**1** gives only the left-handed Λ-enantiomers (Figure 2c). In this

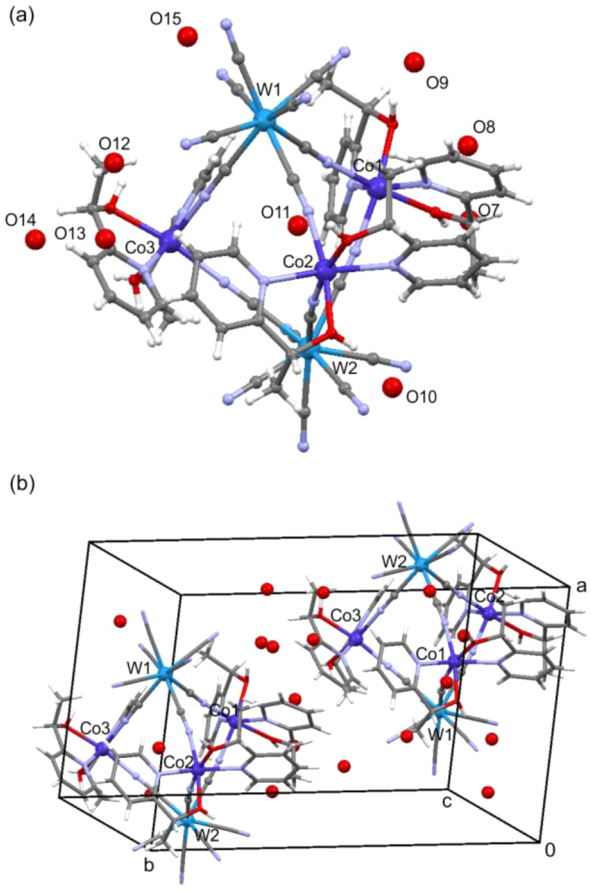

Figure 1. Crystal structures of (*R*)-**1**: the asymmetric unit with the numbering of the W, Co, and O_{water} atoms (a) and the contents of one crystallographic cell (b). Atom color code: navy blue, Co; cyan, W; pale blue, N; gray, C; red, O; white, H.

manner, a tendency of trigonal bipyramids toward ΔΔΔ or ΛΛΛ homochirality was accommodated to form a pair of chiral molecular networks. Moreover, three different Co−NC−W linkages toward two different $[W(CN)_8]$ moieties were afforded. A good illustration of the chirality in (*S*)- and (*R*)-**1** is provided by continuous chirality measure (CCM) analysis for distinguishable molecular fragments *cis*-$[Co(\mu\text{-}NC)_2(mpm)_2]$, $[W(CN)_8][Co(\mu\text{-}NC)_2(mpm)_2]$, and $[W(CN)_8]$ (Table S4 in the SI).[61] The overall organic and coordination homochirality of $\{Co_3W_2\}$ molecules spreads to the whole crystal through supramolecular interactions and contacts. These are dominated by hydrogen bonding with H_2O (Figures 3 and 4), coexisting and cooperating with intra- and intermolecular contacts between terminal CN^- ligands and hydrogen, methyl, and pyridine groups of mpm (Figure S3a in the SI). Notably, the hydrogen groups at C* chirality centers stand outside the molecule perpendicular to the W1−W2 axis, while the methyl groups are oriented almost parallel to the nearest W−CN−Co linkages of the same molecule (Figure S3b in the SI).

The crystal structure is definitely stabilized by a hydrogen-bonding network, involving crystallization of H_2O molecules, R−OH groups of the mpm ligands, and N atoms of the $[W(CN)_8]^{3-}$ moiety. A striking feature of the hydrogen-bonding network is the nonequivalency of the supramolecular interactions in the vicinity of Co1 or Co2 with respect to Co3 centers (Figure 3 and Table S5 in the SI), which is in line with

DOI: 10.1021/acs.inorgchem.5b00470
Inorg. Chem. 2015, 54, 5784−5794

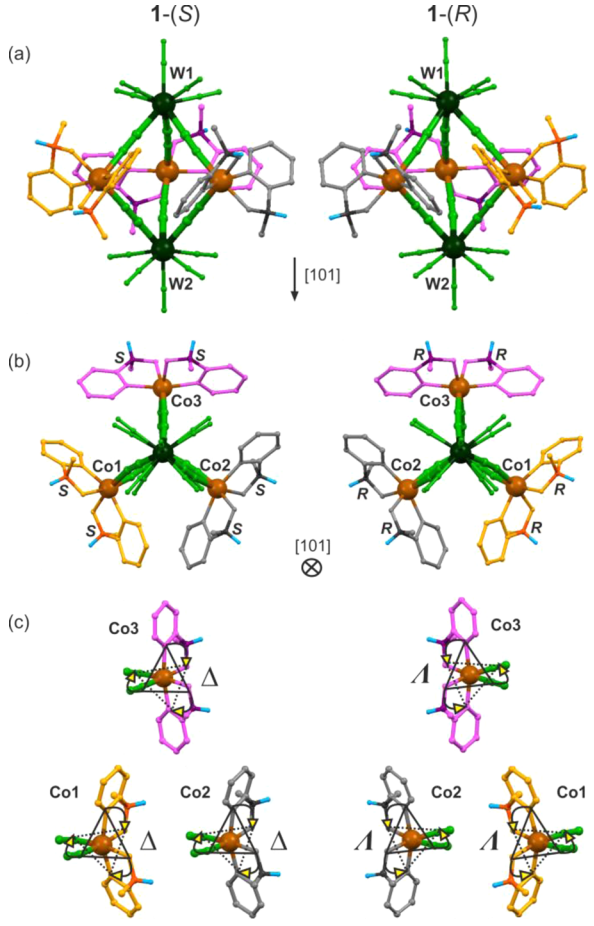

Figure 2. Chirality of molecular structures of Co_3W_2 in (*S*)- and (*R*)-**1**: perpendicular (a) and parallel (b) views with respect to the [101] axis. (c) Homochirality of *cis*-$[Co(\mu\text{-}NC)_2(mpm)_2]$ units. H_2O molecules were omitted for clarity.

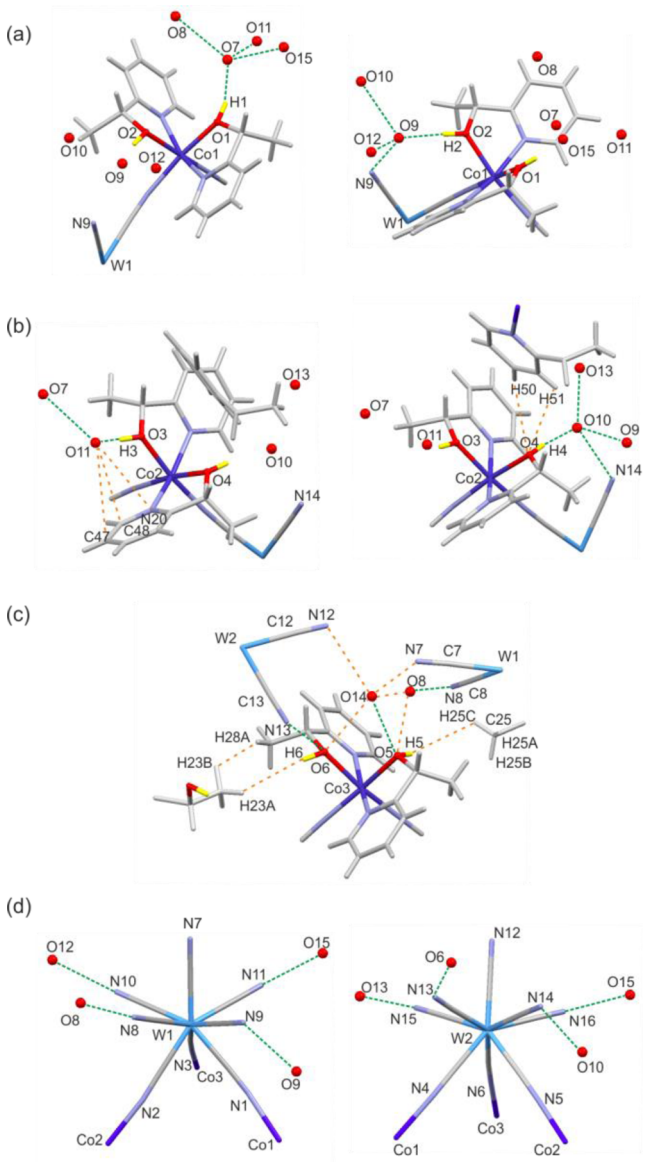

Figure 3. Hydrogen-bonding (green dashed lines) and weak intermolecular interactions or contacts (orange dashed lines) in the vicinity of the Co1 (a), Co2 (b) Co3 (c), and W (d) centers. Atom color code: navy blue, Co; cyan, W; pale blue, N; red, O; yellow, $H_{OH,mpm}$; gray, C and $H_{py,mpm}$.

the observed distortion from the ideal TBP shape of Co_3W_2. A detailed description of these supramolecular interactions is included in the SI.

Within the molecular architecture of (*R*)- and (*S*)-**1**, two groups of H_2O molecules can be distinguished (Figures 4 and S4 in the SI with a detailed description). The five H_2O molecules located at O7, O8, O11, O14, and O15 sites are arranged along the open channel running parallel to the *a* crystallographic direction and can be regarded as weakly bonded. The four remaining molecules represented by O9, O10, O12, and O13 atoms are arranged into squares and reside in the separate cages formed by surrounding $[W(CN)_8]^{3-}$ and mpm fragments. In contrast to the previous ones, they are regarded as strongly bonded. Interestingly, both types of H_2O molecules form *separate* and *independent* hydrogen-bonding systems.

The hydrogen-bonding scheme is in good agreement with the TGA/QMS data (Figure 4b). Two regions of weight loss assigned to H_2O removal were distinguished. The first weight loss of 4.6% occurs in the range of 25−60 °C (maximum in the QMS signal at 42 °C) and can be assigned to five H_2O molecules (theoretical 4.8%). The second weight loss of 4.0% occurs in the range of 60−125 °C (maximum in the QMS signal at 87 °C) and is assigned to four H_2O molecules (theoretical 3.9%). Neither the cyanide-related fragments nor the mpm-related fragments were detected in this temperature region.

Optical Properties. The representative UV/vis diffuse-reflectance and NCD spectra of (*R*)- and (*S*)-**1** are presented in Figure 5. The UV/vis spectrum was deconvoluted into seven components centered at 223 (A), 274 (B), 330 (C), 370 (D) 479 (E), 554 (F), and 614 (G) nm. Components A and B can be assigned to the intraligand transitions of the mpm ligand[10] as well as to the charge-transfer transitions within $[W(CN)_8]^{3-}$: metal-to-ligand charge-transfer (MLCT) from W to CN^- $[E''(^2B_1) \rightarrow E''(^2B_2)$; $b_2(\pi^*)$ and $E''(^2E)$; $e(\pi^*)]$ (component A) and ligand-to-metal charge-transfer (LMCT) from CN^- to W $[E''(^2B_1)$; $[b_1(x^2-y^2)]^1 \rightarrow E''(^2B_1)$; $b_1[b_1(x^2-y^2)]^2]$ (component B).[62] The components C and D can be assigned only to $[W^V(CN)_8]^{3-}$, revealing LMCT character: $E''(^2B_1) \rightarrow E''(^2E)$; $e^3[b_1(x^2-y^2)]^2$ (peak C), $E''(^2B_1) \rightarrow E'(^2E)$; $e^3[b_1(x^2-y^2)]^2$, and $E'(^2A_2)$; $a_2[b_1(x^2\text{-}y^2)]^2$ (peak D).[62] The UV part of

DOI: 10.1021/acs.inorgchem.5b00470
Inorg. Chem. 2015, 54, 5784−5794

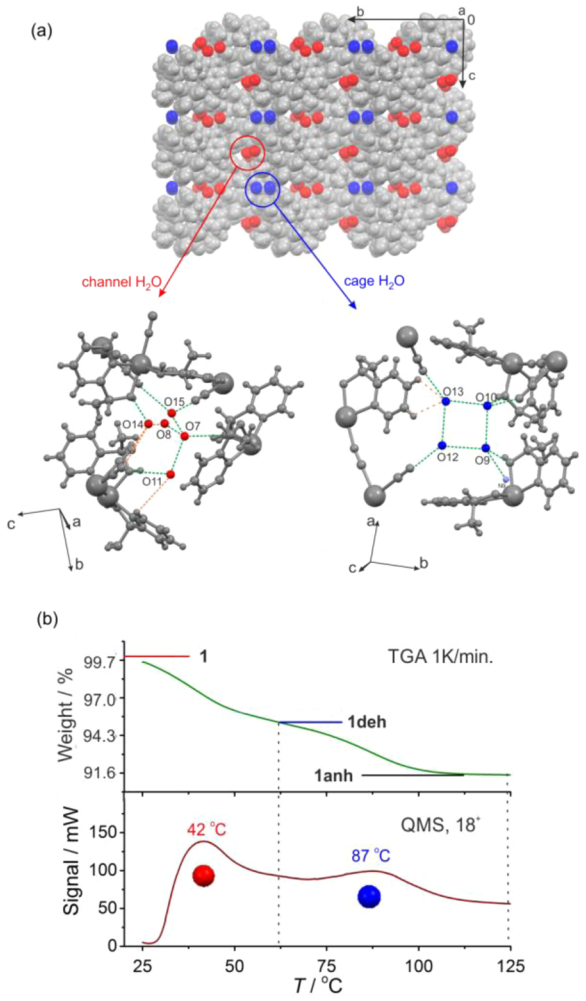

Figure 4. (a)Two types of crystallization H_2O molecules in (*R*)- and (*S*)-**1** and (b) TGA/QMS data in the range of 25−125 °C (dT/dt = 1 K·min^{-1}). Color code: channel H_2O, red; cage H_2O, blue; other atoms, gray; green dotted lines, hydrogen bonds; orange dotted lines, intermolecular contacts.

the spectrum contains also the contributions from ligand-field (LF) transitions of W^V and from charge-transfer transitions of $[Co(\mu\text{-}NC)_2(mpm)_2]$ moieties. The components E−G are of the different origins. Peak E is attributed to metal-to-metal charge transfer (MMCT) from Co^{II}_{HS} to W^V,[63] while peaks F and G are assigned to d−d transitions in high-spin Co^{II}, $^4T_{1g}(^4F) \rightarrow {}^4T_{1g}(^4P)$, and $^4T_{1g}(^4F) \rightarrow {}^4A_{2g}(^4F)$, respectively.[64] The NCD spectra of (*R*)- and (*S*)-**1** are complementary to each other in the whole examined 200−700 nm wavelength region, which confirms the enantiopurity of both materials and indicates nonzero optical activity within all absorption bands. The spectra are dominated by a relatively strong Cotton effect in the range 400−600 nm, positive for (*R*)-**1** and negative for (*S*)-**1**, indicating strong optical activity on $[Co(mpm)_2(NC)_2]$ units within the LF and MMCT absorption bands. The overall NCD spectra indicate that the chirality was successfully transferred toward the whole molecule and crystal lattice, in accordance with CCM analysis (Table S4 in the SI).

Magnetic Properties. Both enantiomers (*R*)- and (*S*)-**1** reveal identical magnetic properties; therefore, only the results for (*R*)-**1** are presented (depicted later as **1** in Figure 6). Because of the sensitivity to dehydration at room temperature,

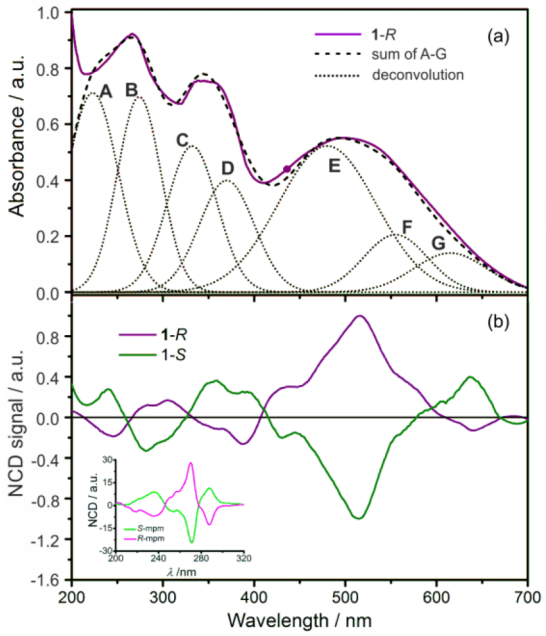

Figure 5. (a) Electronic and (b) NCD spectra of (*R*)- and (*S*)-**1**. Inset: NCD spectra of (*R*)- and (*S*)-mpm.

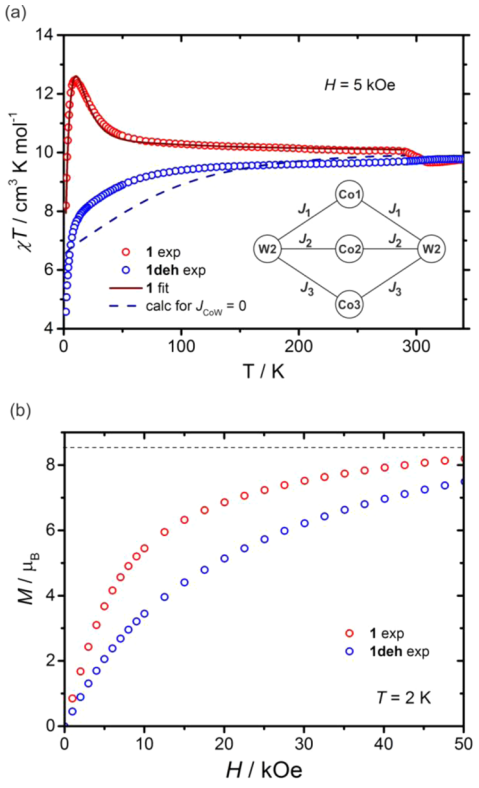

Figure 6. (a) Magnetic properties of **1** and **1deh** [here illustrated for the (*R*)-**1** analogue]: (i) $\chi_M T(T)$ dependence for **1** (red circles) together with the curve fitted using the J_1, J_2, and J_3 magnetic interactions model (inset) with a zJ' contribution (brown line); (ii) $\chi_M T(T)$ dependence for **1deh** (blue circles) together with the curve calculated without the exchange interaction included, i.e., showing only the contribution coming from individual ions (navy dashed line). It was necessary to include the prefactor of 0.93 to get an agreement between the experimental and fitted data. (b) $M(H)$ dependencies.

DOI: 10.1021/acs.inorgchem.5b00470
Inorg. Chem. 2015, 54, 5784−5794

the magnetic properties of **1** were investigated within the limited 2−290 K range. The $\chi_M T$ product at 290 K is 9.9 $cm^3 \cdot mol^{-1} \cdot K$ for the $\{Co^{II}_3W^V_2\}$ unit, which falls within the range of 8.8−10.9 $cm^3 \cdot mol^{-1} \cdot K$ expected for uncoupled magnetic moments of three octahedral high-spin cobalt(II) complexes (S_{Co} = $^3/_2$; g_{Co} = 2.4−2.7)[63] and two $[W^V(CN)_8]^{3-}$ ions, assuming S_W = $^1/_2$ and g_W = 1.97.[5,33,66−68] With decreasing temperature, the $\chi_M T$ signal grows gradually to a maximum value of 12.4 $cm^3 \cdot mol^{-1} \cdot K$ at 10 K and later decreases fast, reaching 8.1 $cm^3 \cdot mol^{-1} \cdot K$ at 2 K (Figure 6a). The continuous increase of $\chi_M T$ is definitely attributed to intracluster cyanido-mediated Co^{II}−W^V magnetic coupling, while the low-temperature decrease of $\chi_M T$ can be related to the single-ion properties of Co^{II} centers or the influence of antiferromagnetic intercluster interactions. The continuous increase of $\chi_M T$ observed even at relatively high temperature suggests that the magnetic exchange interaction in **1** is of a predominant ferromagnetic character, typically detected for bimetallic $Co^{II}[W^V(CN)_8]^{3-}$ magnetic systems.[5,33,67−69] In fact, the maximum on the $\chi_M T$−T plot of 12.4 $cm^3 \cdot mol^{-1} \cdot K$ at 10 K is close to the value of 12.6 $cm^3 \cdot mol^{-1} \cdot K$ expected for the ferromagnetic $\{Co^{II}_3W^V_2\}$ cluster with an effective ground-state spin of S_F = $^5/_2$ and an average g value of 3.4, derived from S_W = $^1/_2$ and g_W = 1.97 and the effective parameters of S = $^1/_2$ and g = 4.3 predicted for octahedral Co^{II} in the low-temperature regime.[65,66] The magnetization of **1** measured as a function of the external magnetic field at 2 K does not saturate to 50 kOe, reaching a value of 8.0 μ_B, but tends roughly in an asymptotic manner limit of 8.5 μ_B, which is expected for ferromagnetic alignment of Co^{II} and W^V magnetic moments within the $\{Co^{II}_3W^V_2\}$ units (Figure 6b).[5,33,67] There is no detectable signal in the out-of-phase magnetic susceptibility above 1.8 K precluding the SMM behavior of **1**.

Ab Initio Calculations. To get insight into the nature of intracluster Co^{II}−W^V magnetic coupling in **1**, consideration of the single-ion properties of three different cobalt(II) complexes embedded in the molecular structure of **1** is of great importance because their significant magnetic anisotropy can strongly influence the magnetic interaction with other metal centers.[65] Thus, we performed ab initio calculations for Co^{II} fragments based on the available structural data, and the results are shown in Table 2 and Tables S6−S9 and Figures S5 and S6 in the SI. The first excited states are close to the ground state for all three Co^{II} centers, which shows that spin−orbit coupling strongly mixes these states. As a result, a large zero-field splitting (ZFS) is obtained. CASPT2 calculation does not decrease the ZFS on Co sites, which shows that its large value is related to the structure but not to the lack of dynamical correlation effects. The local magnetic easy axes of the Co centers are shown in Figure 7, while the full set of spin-free states, spin−orbit energies, and **g** tensors of the ground Kramers doublet for all three symmetrically independent Co1, Co2, and Co3 centers are presented in Table 2.

Using the results of ab initio calculations and the experimental $\chi_M T(T)$ data, we then attempted to calculate the strength of magnetic interactions within the Co−NC−W linkages. Because the whole $\{Co_3W_2\}$ cluster is symmetrically independent, six exchange coupling parameters should be taken into account. However, for the sake of simplicity and to avoid overparametrization, the Heisenberg Hamiltonian using only the three magnetic coupling constants J_1, J_2, and J_3 was employed, according to the following simplified model:

Table 2. Spin-Free States, Spin−Orbit Energies, and g Tensors of the Ground Kramers Doublet in (*R*)-1

magnetic center	Co1	Co1 CASPT2	Co2	Co3
spin-free states originating from the quartet spin state, cm^{-1}	0	0	0	0
	134	423	333	240
	739	917	1194	1056
	7626	9006	7307	7723
	8037	9604	7758	8031
	8673	10942	8134	8627
spin−orbit energies, cm^{-1}	0	0	0	0
	235	187	189	224
	468	593	577	510
	820	853	860	828
	1214	1296	1543	1452
	1315	1362	1631	1537
g_x	2.44	2.04	1.88	1.94
g_y	2.91	2.67	2.41	2.63
g_z	7.15	7.33	7.71	7.58

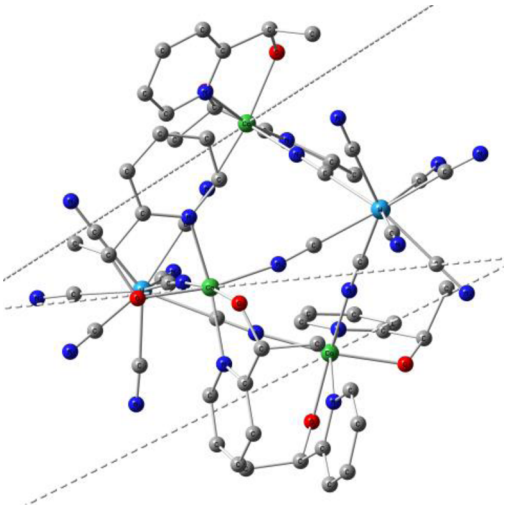

Figure 7. Orientation of the local magnetic axes of the Co centers in (*R*)-**1**. Color code: red, O; blue, N; green, Co; cyan, W; gray, C.

$$\hat{H}_{exch} = -J_1\hat{S}_{Co1}\cdot\hat{S}_{W1} - J_1\hat{S}_{Co1}\cdot\hat{S}_{W2} - J_2\hat{S}_{Co2}\cdot\hat{S}_{W1} - J_2\hat{S}_{Co2}\cdot\hat{S}_{W2} - J_3\hat{S}_{Co3}\cdot\hat{S}_{W1} - J_3\hat{S}_{Co3}\cdot\hat{S}_{W2}$$

The additional zJ' contribution from the intermolecular interactions, mediated by the hydrogen-bonding network, was also added. The exchange interaction was considered within the Lines model on the basis of the resulting spin−orbital multiplets of individual calculated Co centers. The best fitting of the magnetic susceptibility is provided by the exchange coupling constants: J_1 = 10.0 cm^{-1}; J_2 = 1.0 cm^{-1}; J_3 = 15.0 cm^{-1}; zJ' = −0.1 cm^{-1} (Figure 6a). This confirms the ferromagnetic nature of intracluster Co^{II}−W^V coupling in **1**, consistent with other reports on cyanido-bridged Co^{II}−W^V magnetic systems,[66,68,69] which is accompanied by typical weak antiferromagnetic intermolecular magnetic interactions. Such different nature of magnetic interactions was previously suggested for other cyanido-mediated Co^{II}−W^V magnetic systems, consisting also of three slightly different octahedral Co sites.[5] However, the fitted parameters J_1 and J_3 are larger than those found for similar cyanide-bridged W−Co com-

DOI: 10.1021/acs.inorgchem.5b00470
Inorg. Chem. 2015, 54, 5784−5794

pounds.[68,69] We suggest that the relatively large values of J_1 and J_3 could appear because of the large ZFS on Co sites.

Dehydration-Driven Structural Phase Transition. The occurrence of the dehydration-driven structural change **1** → **1deh**, according to the relatively easy partial removal of crystallization H_2O molecules from the intercluster space (TGA/QMS data; Figure 4) leads to a significant change in the magnetic characteristics. The heating of **1** in SQUID above 290 K (17 °C) led to a small decrease of $\chi_M T$ from 9.9 to 9.6 $cm^3 \cdot K \cdot mol^{-1}$ at 310 K (37 °C), which is still within the range of 8.8–10.9 $cm^3 \cdot mol^{-1} \cdot K$ predicted for an uncoupled $\{Co^{II}_3W^{V}_2\}$ unit, assuming $S_{Co} = {}^3/_2$, $g_{Co} = 2.4–2.7$,[63] $S_W = {}^1/_2$, and $g_W = 1.97$.[3,31,65,66] As a result of this transition, it can be expected that the Co^{II} centers are slightly deformed, which gives a decrease of their g values (from average 2.55 to 2.51) and a consequent decrease of the magnetic signal.[65] The sample of **1deh**, obtained by annealing **1** to T = 340 K (67 °C) during magnetic measurements, was subsequently cooled, and the susceptibility measurement was performed (Figure 6, blue points). With decreasing temperature, the $\chi_M T$ product gradually decreases, first slowly and below 10 K very fast, reaching a value of 4.5 $cm^3 \cdot mol^{-1} \cdot K$ at 2 K. This is in contrast with the properties of hydrated form **1** showing a maximum on the $\chi_M T–T$ plot (Figure 6). The magnetization $M(H)$ for **1deh** measured at 2 K is also significantly lower in comparison to that of **1**. In the low-field range below 10 kOe, it increases slower with increasing field, and the curve reaches at 50 kOe the value of 7.2 μ_B, much lower than 8.0 μ_B for **1**. All of these features suggest that the transition **1** → **1deh** changes the Co^{II} single-ion properties and strongly influences the $Co^{II}–W^{V}$ magnetic coupling.

The dehydration process is reversible, which is illustrated by convergence of the $\chi_M T(T)$ and $M(H)$ curves measured in the first cycle with the related curves measured in the second cycle, after exposure of **1deh** to a drop of water and drying at room temperature (Figure S7 in the SI). To better understand the correlation between the magnetic characteristics and dehydration-driven phase transition from **1** to **1deh**, we performed variable-temperature powder XRD measurements and IR and UV/vis diffuse-reflectance spectroscopic studies, which are confronted with the crystal structure of **1**.

The heating of **1** above ca. 50 °C under normal pressure conditions leads to the dark-orange microcrystalline phase **1deh** (Figure S8 in the SI). The monocrystallinity is lost at this stage because of microcracks occurring in the crystal. The dark-crimson color is recovered after exposure to moisture. Heating above 125 °C gives a brown hydrophobic residue, **1anh**, which was not further characterized. The variable-temperature powder diffractograms measured under thermally stabilized conditions are presented in Figure 8. The powder diffractograms at 25 and 36 °C are consistent with those calculated from the monocrystalline data for the original (*R*)- and (*S*)-**1**. The mixed-phase pattern combining the peaks of **1** and **1deh** was observed at 47 °C, while at 57 °C, the pure diffractogram of partially dehydrated phase **1deh** evolved. The observed transition is reversible because the powder diffractogram of **1** was recovered during cooling to room temperature. Further heating up to 107 °C did not lead to a change of the powder pattern, while above this temperature, a second, irreversible transition to the amorphous phase was detected.

The powder XRD pattern of **1deh** was indexed in the $P2_1$ space group, with the following novel cell parameter set: a = 13.6609 Å, b = 20.6149 Å, c = 13.5796 Å, β = 106.2197°, and V = 3672 Å^3. A notable decrease of the crystallographic cell volume ΔV of 212 Å^3 was observed during the transition from **1** (3884 Å^3) to **1deh** (3672 Å^3). This is consistent with the loss of four to seven H_2O molecules per $\{Co_3W_2\}$ unit of **1**[70] and in a good agreement with the presence of five weakly bonded channel H_2O molecules indicated in the crystal structure of **1** (Figure 4). Moreover, a comparison with the cell parameters of **1** [a = 13.645(3) Å, b = 19.826(4) Å, c = 14.811(3) Å, and β = 104.18(3); $P2_1$ space group] indicates that the structural changes include cell deformation with a moderate elongation in the b direction (~0.8 Å, ~3.9%) and more serious shrinkage along the c direction (~1.2 Å, 8.8%). This is in line with the plausible movements of whole $\{Co_3W_2\}$ clusters, aiming to reoccupy the empty spaces generated by the removal of channel H_2O molecules located at the O7, O8, O11, O14, and O15 sites (Figure 9). Going further, such movements can be responsible for the opening of cages, which allows the removal of cage H_2O molecules located at the O9, O10, O12, and O13 sites. The thermal evolution and conditions of reversibility of powder XRD patterns indicate the relative stability of the molecular architecture of the **1** and **1deh** phases in spite of the rather continuous character of the removal/sorption of H_2O.

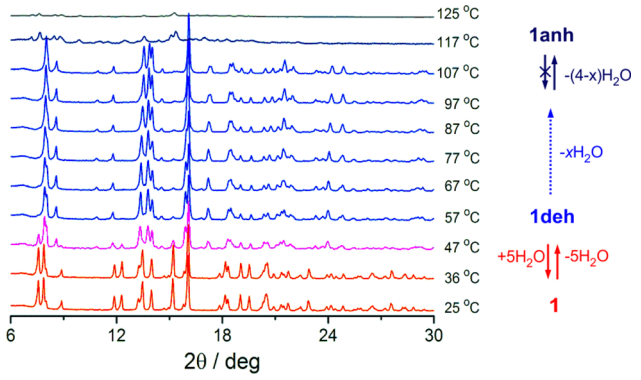

Figure 8. Variable-temperature powder XRD (thermal stabilization mode) and the proposed scheme for the compositional changes during the dehydration/rehydration processes in **1**.

Unfortunately, because of the low symmetry and large asymmetric unit of **1deh**, the complete crystal structure analysis of **1deh** as well as exact magnetostructural correlations were precluded. However, on the basis of the above consideration, we infer that the drastic change in the magnetic characteristics during the transition **1** → **1deh** is related to substantial modifications of the clusters' core and their supramolecular arrangement. Such modifications significantly change the single-ion properties of Co^{II} ions including the change of the ZFS properties as well as the SOC and resulting directions of the g anisotropy axes. It was suggested before that local hydrogen bonding involving the R–OH groups of the mpm ligands around the Co1 and Co2 ions is significantly different from that around Co3 (Figure 3). The removal of weakly bonded O7, O8, O11, O14, and O15 H_2O molecules and the **1** → **1deh** transition strongly affect the binding of mpm "wings" at the Co1 and Co2 centers. The plausible altering of chelate twisting at the *cis*-$[Co(mpm)_2(\mu\text{-}NC)_2]$ moiety influences its geometry and, hence, the single-ion properties. The dehydration presumably also influences the geometry and lengths of the cyanide bridges and solvent-controlled intercluster distances. All of these changes obviously significantly affect both the intra- and intercluster magnetic interactions. The $\chi_M T(T)$ plot for the dehydrated phase is much below the curve

DOI: 10.1021/acs.inorgchem.5b00470
Inorg. Chem. 2015, 54, 5784–5794

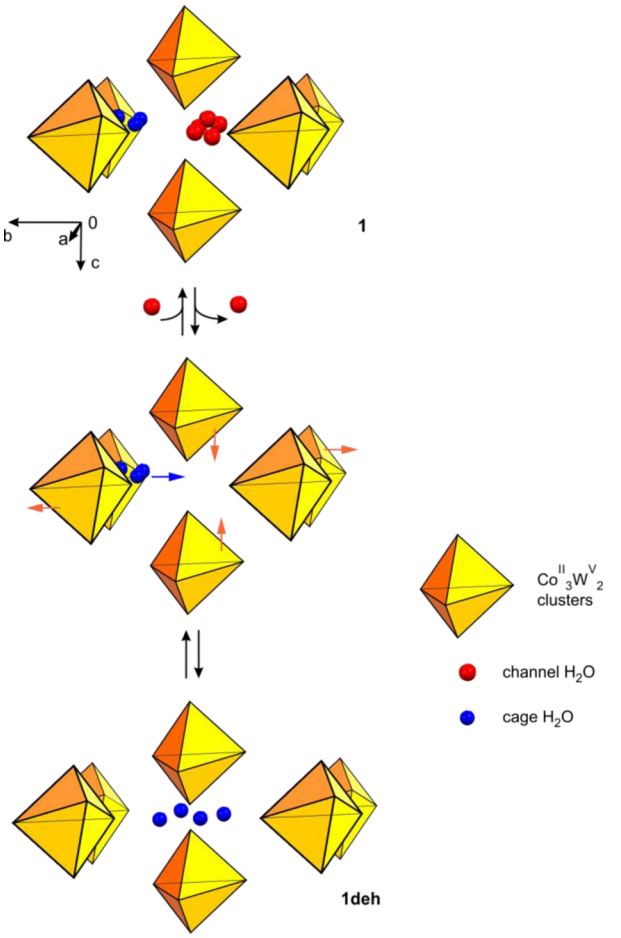

Figure 9. Schematic representation of structural changes during the dehydration/rehydration processes in **1**. The blue arrows show the directions of molecular movements.

for the hydrated phase, but the signal is still higher than the combined contributions from the individual Co^{II} and W^{V} centers without any exchange interactions (in T below 200 K), which suggests that ferromagnetic coupling also operates in **1deh** (Figure 6a). However, dehydration-induced structural modifications cause a decrease in the strength of ferromagnetic Co^{II}–W^{V} coupling, which can also be accompanied by the increasing contribution from the antiferromagnetic intermolecular correlation related to the decreasing intercluster distances.

The above considerations assume retention of the composition and topology of the $\{Co_3W_2\}$ cluster during the transition **1** → **1deh**. This is confirmed by only a minor change in the variable-temperature IR spectra in the ν(CN) range, indicating stability of the W^{V} valence state,[71] and is in agreement with a minor modification of the interaction of CN^{-} ligands with crystallization of H_2O and mpm (Figure S8a in the SI; see also Figure 3d). A significant change in the variable-temperature reflectance spectra suggests a more pronounced modification in the electronic structure of $(\mu\text{-NC})_2Co^{II}(mpm)_2$ moieties (CT and LF bands of Co^{II}; MMCT $W^{V} \rightarrow Co^{II}$)[63,64] due to the major modification of interactions $_{mpm}O\cdots O_{water}$ (Figure S8b in the SI; see also Figure 3). The occurrence of a charge-transfer effect, giving the Co^{III}–W^{IV} pair, can be excluded.[17]

CONCLUSIONS

Realizing the concept of implementation of chirality into a magnetic skeleton, we have prepared a novel pair of enantiomorphic (R)- and (S)-**1** cyanido-bridged cluster-based materials. The material displayed for the first time the combination of structural chirality and resulting natural optical activity with a magnetic spongelike behavior in the unique $\{Co_3W_2\}$-based supramolecular network exploiting the archetypal cyanido-bridged TBP molecular structure. The underlying reversible dehydration-driven structural phase transition between **1** and **1deh** occurs directionally as a consequence of the partial removal/uptake of specifically located crystallization H_2O molecules. The structural changes involve mainly minor alterations in the geometry of a cluster core and a major modifications in the supramolecular network, including the hydrogen-bonding scheme in the vicinity of $[Co^{II}(mpm)_2(\mu\text{-NC})_2]$ moieties. These features result in changes of the Co^{II} single-ion properties and a subsequent decrease in the strength of the ferromagnetic interactions, together with increasing antiferromagnetic intercluster coupling. The "magnetic sponge" mechanism based on the strong correlation between the hydrogen-bonding scheme and magnetic parameters is in line with the ab initio results of theoretical investigations. Presented materials demonstrate a new interesting pathway in the research of functional magnetic-cluster-based solids, and a few promising possibilities, including the uptake of guest molecules and a study of their prospective influence on the magnetic and magnetooptical properties of **1**, will be the subject of a future work.

ASSOCIATED CONTENT

Supporting Information

Crystallographic data [CIF files; CCDC 1051001 for (R)-**1** and 1051002 for (S)-**1**], detailed structural tables and figures, continuous shape measurements (CSM) and CCM results, detailed figures and tables related to ab initio methods and results, reversibility of $\chi_M T(T)$ and $M(H)$ data, variable-temperature IR spectra of (R)-**1** in the ν(CN) region, and variable-temperature visible reflectance spectra of (R)-**1**. The Supporting Information is available free of charge on the ACS Publications website at DOI: 10.1021/acs.inorgchem.5b00470.

AUTHOR INFORMATION

Corresponding Author

*E-mail: robert.podgajny@uj.edu.pl.

Author Contributions

The manuscript was written through contributions of all authors. All authors have given approval to the final version of the manuscript.

Notes

The authors declare no competing financial interest.

ACKNOWLEDGMENTS

The authors thank Prof. Z. Tomkowicz (Jagiellonian University, Kraków, Poland) for access to the NCD spectrometer purchased with support of the European Regional Development Fund within the Polish Innovation Economy Operational Program (POIG.02.01.00-12-023/08). We also thank Prof. T. Łojewski (Jagiellonian University, Kraków, Poland) for access to the AvaSpec-2048 spectrometer and for his help in recording the reflectance spectra. We thank Prof. B. Machura (Silesia University, Katowice, Poland) for single crystal XRD measure-

DOI: 10.1021/acs.inorgchem.5b00470
Inorg. Chem. 2015, 54, 5784–5794

ments for (*S*)-**1**. This work was supported by the International Ph.D. Studies Programme at the Faculty of Chemistry, Jagiellonian University, within the Foundation for Polish Science MPD Programme, cofinanced by the EU European Regional Development Fund and by the Polish National Science Centre within Project DEC-2011/01/B/ST5/00716. S.C. gratefully acknowledges financial support of the Foundation for Polish Science within the START fellowship (edition 2014).

REFERENCES

(1) Train, C.; Gruselle, M.; Verdaguer, M. *Chem. Soc. Rev.* **2011**, *40*, 3297−3312.
(2) Coronado, E.; Mínguez Espellagras, G. *Chem. Soc. Rev.* **2013**, *42*, 1525−1539.
(3) Tokoro, H.; Ohkoshi, S. *Dalton Trans.* **2011**, *40*, 6825−6833.
(4) Nowicka, B.; Korzeniak, T.; Stefańczyk, O.; Pinkowicz, D.; Chorazy, S.; Podgajny, R.; Sieklucka, B. *Coord. Chem. Rev.* **2012**, *256*, 1946−1971.
(5) Chorazy, S.; Nakabayashi, K.; Imoto, K.; Mlynarski, J.; Sieklucka, B.; Ohkoshi, S. *J. Am. Chem. Soc.* **2012**, *134*, 16151−16154.
(6) Chorazy, S.; Nakabayashi, K.; Ozaki, N.; Pełka, R.; Fic, T.; Mlynarski, J.; Sieklucka, B.; Ohkoshi, S. *RSC Adv.* **2013**, *3*, 1065−1068.
(7) Chorazy, S.; Nakabayashi, K.; Arczyński, M.; Pełka, R.; Ohkoshi, S.; Sieklucka, B. *Chem.—Eur. J.* **2014**, *20*, 7144−7159.
(8) Ohkoshi, S.; Takano, S.; Imoto, K.; Yoshikiyo, M.; Namai, A.; Tokoro, H. *Nat. Photonics* **2014**, *8*, 65−71.
(9) Inoue, K.; Kikuchi, K.; Ohba, M.; Okawa, H. *Angew. Chem., Int. Ed.* **2003**, *42*, 4810−4813.
(10) Chorazy, S.; Podgajny, R.; Nitek, W.; Fic, T.; Görlich, E.; Rams, M.; Sieklucka, B. *Chem. Commun.* **2013**, *49*, 6731−6733.
(11) Pinkowicz, D.; Podgajny, R.; Nitek, W.; Rams, M.; Majcher, A. M.; Nuida, T.; Ohkoshi, S.; Sieklucka, B. *Chem. Mater.* **2011**, *23*, 21−31.
(12) Ohkoshi, S.; Tokoro, H.; Matsuda, T.; Takahashi, H.; Irie, H.; Hashimoto, K. *Angew. Chem., Int. Ed.* **2007**, *46*, 3238−3241.
(13) Ohkoshi, S.; Nakagawa, K.; Tomono, K.; Imoto, K.; Tsunobuchi, Y.; Tokoro, H. *J. Am. Chem. Soc.* **2010**, *132*, 6620−6621.
(14) DaSilva, J. G.; Miller, J. S. *Inorg. Chem.* **2013**, *52*, 1418−1423.
(15) Ohtani, R.; Yoneda, K.; Furukawa, S.; Horike, N.; Kitagawa, S.; Gaspar, A. B.; Carmen Munoz, M.; Real, J. A.; Ohba, M. *J. Am. Chem. Soc.* **2011**, *133*, 8600−8605.
(16) Dechambenoit, P.; Long, J. R. *Chem. Soc. Rev.* **2011**, *40*, 3249−3265.
(17) Ozaki, N.; Tokoro, H.; Hamada, Y.; Namai, A.; Matsuda, T.; Kaneko, S.; Ohkoshi, S. *Adv. Funct. Mater.* **2012**, *20*, 2089−2093.
(18) Avendano, C.; Hilfiger, M. G.; Prosvirin, A.; Sanders, C.; Stepien, D.; Dunbar, K. R. *J. Am. Chem. Soc.* **2010**, *132*, 13123−13125.
(19) Ohkoshi, S.; Tokoro, H. *Acc. Chem. Res.* **2012**, *45*, 1749−1758.
(20) Ohkoshi, S.; Arai, K.; Sato, Y.; Hashimoto, K. *Nat. Mater.* **2004**, *3*, 857−861.
(21) Ohkoshi, S.; Tsunobuchi, Y.; Takahashi, H.; Hozumi, T.; Shiro, M.; Hashimoto, K. *J. Am. Chem. Soc.* **2007**, *129*, 3084−3085.
(22) Pinkowicz, D.; Podgajny, R.; Gaweł, B.; Nitek, W.; Łasocha, W.; Oszajca, M.; Makarewicz, M.; Bałanda, M.; Sieklucka, B. *Angew. Chem., Int. Ed.* **2011**, *50*, 3973−3977.
(23) Pinkowicz, D.; Podgajny, R.; Nowicka, B.; Chorazy, S.; Reczyński, M.; Sieklucka, B. *Inorg. Chem. Front.* **2015**, *2*, 10−27.
(24) Shatruk, M.; Avendano, C.; Dunbar, K. R. In *Progress in Inorganic Chemistry*; Karlin, K. D., Ed.; John Wiley & Sons: Hoboken, NJ, 2009; Vol. *56*, pp 155−334.
(25) Choi, H. J.; Sokol, J. J.; Long, J. R. *Inorg. Chem.* **2004**, *43*, 1606−1608.
(26) Ferbinteanu, M.; Miyasaka, H.; Wernsdorfer, W.; Nakata, K.; Sugiura, K.; Yamashita, M.; Coulon, C.; Clérac, R. *J. Am. Chem. Soc.* **2005**, *127*, 3090−3099.
(27) Karadas, F.; Schelter, E. J.; Shatruk, M.; Prosvirin, A. V.; Bacsa, J.; Smirnov, D.; Ozarowski, A.; Krzystek, J.; Telser, J.; Dunbar, K. R. *Inorg. Chem.* **2008**, *47*, 2074−2082.
(28) Nihei, M.; Sekine, Y.; Suganami, N.; Nakazawa, K.; Nakao, A.; Nakao, H.; Murakami, Y.; Oshio, H. *J. Am. Chem. Soc.* **2011**, *133*, 3592−3600.
(29) Li, D.; Parkin, S.; Wang, G.; Yee, G. T.; Clérac, R.; Wernsdorfer, W.; Holmes, S. M. *J. Am. Chem. Soc.* **2006**, *128*, 4214−4215.
(30) Nihei, M.; Ui, M.; Hoshino, N.; Oshio, H. *Inorg. Chem.* **2008**, *47*, 6106−6108.
(31) Funck, K. E.; Hilfiger, M. G.; Berlinguette, C. P.; Shatruk, M.; Wernsdorfer, W.; Dunbar, K. R. *Inorg. Chem.* **2009**, *48*, 3438−3452.
(32) Song, Y.; Zhang, P.; Ren, X.-M.; Shen, X.-F.; Li, Y.-Z.; You, X.-Z. *J. Am. Chem. Soc.* **2005**, *127*, 3708−3709.
(33) Chorazy, S.; Podgajny, R.; Nitek, W.; Rams, M.; Ohkoshi, S.; Sieklucka, B. *Cryst. Growth Des.* **2013**, *13*, 3036−3045.
(34) Podgajny, R.; Chorazy, S.; Nitek, W.; Rams, M.; Majcher, A. M.; Marszałek, B.; Żukrowski, J.; Kapusta, C.; Sieklucka, B. *Angew. Chem., Int. Ed.* **2013**, *52*, 896−900.
(35) Chorazy, S.; Podgajny, R.; Nogaś, W.; Nitek, W.; Kozieł, M.; Rams, M.; Juszyńska-Gałązka, E.; Żukrowski, J.; Kapusta, C.; Nakabayashi, K.; Fujimoto, T.; Ohkoshi, S.; Sieklucka, B. *Chem. Commun.* **2014**, *50*, 3484−3487.
(36) Shatruk, M.; Dragulusce-Andrasi, A.; Chambers, K. E.; Stoian, S. A.; Bominaar, E. L.; Achim, C.; Dunbar, K. R. *J. Am. Chem. Soc.* **2007**, *129*, 6104−6116.
(37) Wang, C.-F.; Zuo, J.-L.; Bertlett, B. M.; Song, Y.; Long, J. R.; You, X.-Z. *J. Am. Chem. Soc.* **2006**, *128*, 7162−7163.
(38) Gu, Z.-G.; Yang, Q.-F.; Liu, W.; Song, Y.; Li, Y.-Z.; Zuo, J.-L.; You, X.-Z. *Inorg. Chem.* **2006**, *45*, 8895−8901.
(39) Hilfiger, M. G.; Zhao, H.; Prosvirin, A.; Wernsdorfer, W.; Dunbar, K. R. *Dalton Trans.* **2009**, 5155−5163.
(40) Marvilliers, A.; Pei, Y.; Boquera, J. C.; Vostrikova, K. E.; Paulsen, C.; Riviére, E.; Audiére, J.-P.; Mallah, T. *Chem. Commun.* **1999**, 1951−1952.
(41) Vostrikova, K. E.; Luneau, D.; Wernsdorfer, W.; Rey, P.; Verdaguer, M. *J. Am. Chem. Soc.* **2000**, *122*, 718−719.
(42) Berlinguette, C. P.; Vaughn, D.; Canada-Vilalta, C.; Galán-Mascarós, J.; Dunbar, K. R. *Angew. Chem., Int. Ed.* **2003**, *42*, 1523−1526.
(43) Berlinguette, C. P.; Dragulescu-Andrasi, A.; Sieber, A.; Güdel, H.-U.; Achim, C.; Dunbar, K. R. *J. Am. Chem. Soc.* **2005**, *127*, 6766−6779.
(44) Hilfiger, M. G.; Chen, M.; Brinzari, T. V.; Nocera, T. M.; Shatruk, M.; Petasis, D. T.; Musfeldt, J. L.; Achim, C.; Dunbar, K. R. *Angew. Chem., Int. Ed.* **2010**, *49*, 1410−1413.
(45) Funck, K. E.; Prosvirin, A. V.; Mathoniére, C.; Clérac, R.; Dunbar, K. R. *Inorg. Chem.* **2011**, *50*, 2782−2789.
(46) Wang, X.-Y.; Hilfiger, M. G.; Prosvirin, A. V.; Dunbar, K. R. *Chem. Commun.* **2010**, *46*, 4484−4486.
(47) Klokishner, S.; Ostrovsky, S.; Palii, A.; Shatruk, M.; Funcj, K.; Dunbar, K. R.; Tsukerblat, B. *J. Phys. Chem. C* **2011**, *115*, 21666−21677.
(48) Gu, Z.-G.; Yang, Q.-F.; Liu, W.; Song, Y.; Li, Y.-Z.; Zuo, J.-L.; You, X.-Z. *Inorg. Chem.* **2006**, *45*, 8895−8901.
(49) Van Langenberg, K.; Batten, S. R.; Berry, K. J.; Hockless, D. C. R.; Moubaraki, B.; Murray, K. S. *Inorg. Chem.* **1997**, *36*, 5006−5015.
(50) (a) Samotus, A. *Polym. J. Chem.* **1973**, *47*, 653−655. (b) Matoga, D.; Szklarzewicz, J.; Mikuriya, M. *Inorg. Chem.* **2006**, *45* (18), 7100−7104.
(51) Zhou, X.; Wu, X.; Yang, B.; Xiao, J. *J. Mol. Catal. A* **2012**, *357*, 133−140.
(52) (a) Sheldrick, G. M. *Acta Crystallogr., Sect. A: Found. Crystallogr.* **2008**, *64*, 112−122. (b) Sheldrick, G. M. *SHELX97, Programs for Crystal Structure Analysis*, release 97-2; Institut fur Anorganische Chemie der Universitat Gottingen: Gottingen, Germany, 1998. (c) Farrugia, L. J. *J. Appl. Crystallogr.* **1999**, *32*, 837−838. (d) Macrae, C. F.; Edgington, P. R.; McCabe, P.; Pidcock, E.; Shields, G. P.; Taylor,

DOI: 10.1021/acs.inorgchem.5b00470
Inorg. Chem. 2015, 54, 5784−5794

R.; Towler, M.; van de Streek, J. *J. Appl. Crystallogr.* **2006**, *39*, 590−597.
(53) Altomare, A.; Cuocci, C.; Giacovazzo, C.; Moliterni, A.; Rizzi, R.; Corriero, N.; Falcicchio, A. *J. Appl. Crystallogr.* **2013**, *46*, 1231−1235.
(54) Bain, G. A.; Berry, J. F. *J. Chem. Educ.* **2008**, *85*, 532−536.
(55) (a) Chibotaru, L. F.; Ungur, L. *J. Chem. Phys.* **2012**, *137*, 064112(23). (b) Aquilante, F.; De Vico, L.; Ferre, N.; Ghigo, G.; Malmqvist, P.-A.; Neogrady, P.; Pedersen, T. B.; Pitonak, M.; Reiher, M.; Roos, B. O.; Serrano-Andres, L.; Urban, M.; Veryazov, V.; Lindh, R. *J. Comput. Chem.* **2010**, *31*, 224−247. (c) See the *MOLCAS* manual, http://molcas.org/documentation/manual/.
(56) Andersson, K.; Malmqvist, P.-A.; Roos, B. O. *J. Chem. Phys.* **1992**, *96*, 1218−1226.
(57) Lines, M. E. *J. Chem. Phys.* **1971**, *55*, 2977−2984.
(58) Chibotaru, L. F.; Ungur, L.; Aronica, C.; Elmoll, H.; Pilet, G.; Luneau, D. *J. Am. Chem. Soc.* **2008**, *130*, 12445−12455.
(59) Llunell, M.; Casanova, D.; Cirera, J., Alemany, M. P.; Alvarez, S. *SHAPE, v. 2.0, Program for the Stereochemical Analysis of Molecular Fragments by Means of Continuous Shape Measures and Associated Tools*; Departament de Química Física, Departament de Química Inorganica, and Institut de Química Teorica i Computacional, Universitat de Barcelona, Barcelona, Spain, 2010.
(60) von Zelewsky, A.; Mamula, O. *J. Chem. Soc., Dalton Trans.* **2000**, 219−231.
(61) Alvarez, S.; Alemany, P.; Avnir, D. *Chem. Soc. Rev.* **2005**, *34*, 313−326.
(62) Isci, H.; Roy Mason, W. *Inorg. Chim. Acta* **2004**, *357*, 4065−4072.
(63) Ohkoshi, S.; Hamada, Y.; Matsuda, T.; Tsunobuchi, Y.; Tokoro, H. *Chem. Mater.* **2008**, *20*, 3048−3054.
(64) Papánková, B.; Boča, R.; Dlháň, L.; Nemec, I.; Titiš, J.; Svoboda, I.; Fuess, H. *Inorg. Chim. Acta* **2010**, *363*, 147−156.
(65) Lloret, F.; Julve, M.; Cano, J.; Ruiz-García, R.; Pardo, E. *Inorg. Chim. Acta* **2008**, *361*, 3432−3445.
(66) Herrera, J. M.; Bleuzen, A.; Dromzee, Y.; Julve, M.; Lloret, F.; Verdaguer, M. *Inorg. Chem.* **2003**, *42*, 7052−7059.
(67) Chorazy, S.; Podgajny, R.; Majcher, A. M.; Nitek, W.; Rams, M.; Suturina, E. A.; Ungur, L.; Chibotaru, L. F.; Sieklucka, B. *CrystEngComm* **2013**, *15*, 2378−2385.
(68) Clima, S.; Hendrickx, M. F. A; Chibotaru, L. F.; Soncini, A.; Mironov, V.; Ceulemans, A. *Inorg. Chem.* **2007**, *46*, 2682−2690.
(69) Pinkowicz, D.; Pełka, R.; Drath, O.; Nitek, W.; Bałanda, M.; Majcher, A. M.; Poneti, G.; Sieklucka, B. *Inorg. Chem.* **2010**, *49*, 7565−7576.
(70) Podgajny, R.; Chorąży, S.; Nitek, W.; Budziak, A.; Rams, M.; Gomez-García, C. J.; Oszajca, M.; Łasocha, W.; Sieklucka, B. *Cryst. Growth Des.* **2011**, *11*, 3866−3867.
(71) Podgajny, R.; Korzeniak, T.; Stadnicka, K.; Dromzée, Y.; Alcock, N. W.; Errington, W.; Kruczała, K.; Bałanda, M.; Kemp, T. J.; Verdaguer, M.; Sieklucka, B. *Dalton Trans.* **2003**, 3458−3468.

DOI: 10.1021/acs.inorgchem.5b00470
Inorg. Chem. 2015, 54, 5784−5794